

# JGR Atmospheres

## RESEARCH ARTICLE

10.1029/2020JD033286

### Special Section:

The land-air coupling over Tibetan Plateau and its global climate effects

### Key Points:

- The fine mode aerosols exhibited strong absorption in summer in the western Tibetan Plateau (TP)
- The absorption of atmospheric aerosols in summer in the western TP might be significantly underestimated at present
- Anthropogenic activities had a large impact on the aerosol concentrations and properties in summer in the western TP

### Supporting Information:

Supporting Information may be found in the online version of this article.

### Correspondence to:

P. Tian,  
[tianpf@lzu.edu.cn](mailto:tianpf@lzu.edu.cn)

### Citation:

Zhang, L., Tang, C., Huang, J., Du, T., Guan, X., Tian, P., et al. (2021). Unexpected high absorption of atmospheric aerosols over a western Tibetan Plateau site in summer. *Journal of Geophysical Research: Atmospheres*, 126, e2020JD033286. <https://doi.org/10.1029/2020JD033286>

Received 14 JUN 2020

Accepted 1 FEB 2021

### Author Contributions:

**Conceptualization:** Lei Zhang, Jianping Huang

**Data curation:** Chenguang Tang, Pengfei Tian, Jinsen Shi, Min Wang, Huiyu Zeng

**Formal analysis:** Chenguang Tang, Pengfei Tian

**Funding acquisition:** Lei Zhang, Jianping Huang, Pengfei Tian

**Investigation:** Lei Zhang, Chenguang Tang, Tao Du, Xu Guan, Pengfei Tian, Jinsen Shi, Xianjie Cao, Zhongwei Huang, Qi Guo, Min Wang, Huiyu Zeng, Feiyang Wang, Pema Dolkar

## Unexpected High Absorption of Atmospheric Aerosols Over a Western Tibetan Plateau Site in Summer

Lei Zhang<sup>1,2</sup> , Chenguang Tang<sup>2</sup>, Jianping Huang<sup>1,2</sup> , Tao Du<sup>2</sup>, Xu Guan<sup>2</sup>, Pengfei Tian<sup>2</sup> , Jinsen Shi<sup>2</sup>, Xianjie Cao<sup>2</sup>, Zhongwei Huang<sup>2</sup>, Qi Guo<sup>2</sup> , Haotian Zhang, Min Wang<sup>2</sup>, Huiyu Zeng<sup>2</sup>, Feiyang Wang<sup>3</sup>, and Pema Dolkar<sup>3</sup>

<sup>1</sup>Collaborative Innovation Center for Western Ecological Safety, Lanzhou University, Lanzhou, China, <sup>2</sup>Key Laboratory for Semi-Arid Climate Change of the Ministry of Education, College of Atmospheric Sciences, Lanzhou University, Lanzhou, China, <sup>3</sup>Ali Meteorological Administration, Ali, China

**Abstract** The assessment of atmospheric aerosol radiative effects in the Tibetan Plateau (TP) suffers from large uncertainties due to limited understanding of aerosol physicochemical properties. To quantify aerosol optical properties, size distributions, and chemical compositions in the western TP, an intensive field campaign was carried out at Shiquanhe National Reference Climatological Station from July 8 to August 2, 2019. Unexpected low single scattering albedo (SSA) at 870 nm was found for the fine aerosols with an average value of  $0.73 \pm 0.18$ . SSA was even lower than 0.60 in the morning when fine aerosols peaked, indicating high absorption of the fine aerosols induced by anthropogenic activities. Coarse mode aerosols accounted for  $70.58\% \pm 14.98\%$  of the total volume concentration and mineral dust was the most abundant species in total suspended particles with a mass fraction of 48.7%. Fine mode aerosol concentrations showed little dependence on wind speed while coarse mode aerosols and metallic element concentrations exhibited strong positive correlations with wind speed, indicating the importance of wind-blown dust particles. The present study for the first time quantified key aerosol parameters in the western TP and unexpected high absorption of atmospheric aerosols were found over the site in summer. Our results suggest the need to carefully consider the radiative effects caused by aerosol absorption in the TP region.

## 1. Introduction

Atmospheric aerosols in the Tibetan Plateau (TP, also known as the “Third Pole”) play significant roles in earth-atmosphere systems from local to global scales (Yao et al., 2019; Zhao et al., 2018). The geographical conditions and the atmospheric circulation of the TP facilitate the transport of pollutants and water vapor to the global lower stratosphere and upper troposphere (Bian et al., 2020; C. Xu, et al., 2018). Direct radiative effects of absorbing aerosols heat up the air over the TP and consequently affect atmospheric thermodynamics (Lau et al., 2006). Atmospheric aerosols also contribute to precipitation and hydrological cycles in the TP and downstream regions by interacting with clouds (Jin, 2006; Liu et al., 2019). The melting of glaciers and snow cover is accelerated by the deposition of atmospheric aerosols such as black carbon (BC) and mineral dust (MD) (Kang et al., 2019). Long-term remote sensing observations and model simulations reveal that aerosol loading has increased during recent years in most areas of the TP region (Mehta et al., 2019; Zhu et al., 2019).

The understanding of atmospheric aerosols and their effects over the TP is relatively poor despite the importance of the role that aerosols play in the earth-atmosphere systems (Kang et al., 2019; Zhao et al., 2019). For example, long-range transport of biomass burning from South Asia has been widely studied in many researches (Cao et al., 2011; Zhao et al., 2013), while Zhang et al. (2017) suggested that nearby or short-distance sources rather than long-distance transported pollutants are the most important contributors to BC concentrations at a site in the central TP. Long-term CALIPSO (Cloud-Aerosol Lidar and Infrared Pathfinder Satellite Observation) observations showed highest regional average depolarization ratio and color ratio of atmospheric aerosols over the TP in the selected eight regions across China (Tian et al., 2017), indicating the dominance of coarse MD aerosols in this region. But only a small number of the Aerosol Robotic Network (AERONET) sunphotometer observations were classified as dust aerosols (Pokharel et al., 2019). Absorbing aerosols contribute to surface warming in the TP region (Lau et al., 2010; Pepin et al., 2015), but

**Methodology:** Chenguang Tang, Pengfei Tian  
**Project Administration:** Lei Zhang, Jianping Huang, Pengfei Tian  
**Software:** Chenguang Tang, Pengfei Tian  
**Supervision:** Lei Zhang, Jianping Huang  
**Validation:** Lei Zhang, Chenguang Tang, Pengfei Tian  
**Visualization:** Chenguang Tang, Pengfei Tian  
**Writing – original draft:** Chenguang Tang, Pengfei Tian  
**Writing – review & editing:** Lei Zhang, Chenguang Tang, Jianping Huang, Tao Du, Xu Guan, Pengfei Tian, Jinsen Shi, Haotian Zhang

a recent study reveals that air pollution slows down surface warming over the TP (Jia et al., 2020). Aerosol physical properties, chemical compositions, even loading over the TP are poorly quantified due to limited field observations, which might result in higher uncertainty in assessing aerosol effects on weather and climate.

Satellite and ground-based remote sensing data as well as model simulations have been widely used to study spatiotemporal variations and long-range transport of atmospheric aerosols over the TP. Taklimakan desert dust aerosols are transported to the TP region as revealed by CALIPSO and Multiangle Imaging SpectroRadiometer (MISR) observations (Huang et al., 2007; Xia et al., 2008) and WRF-Chem (Weather Research and Forecasting-Chemistry) model simulations (Chen et al., 2013). Aerosol transport and spatial distribution over the TP and downstream regions have been studied by model simulations (Hu et al., 2020; Ji et al., 2015; Liu et al., 2015). Long-term MODIS (Moderate-resolution Imaging Spectroradiometer) data confirms that the northern and western TP regions are influenced by MD aerosols in spring and summer while transported anthropogenic aerosols dominate in the southern and southeastern TP regions (Zhu et al., 2019). Sunphotometer measurements have been used to study column aerosol optical depth at Nam Co, Qomolangma (Mt. Everest), Mt. Waliguan, Lhasa, and Muztagh Ata (Che et al., 2011; Cong et al., 2009; Pokharel et al., 2019; Yan et al., 2015; Zhu et al., 2019). Although satellite and ground-based remote sensing data (e.g., AERONET, MODIS, CALIPSO) are used in various studies on atmospheric aerosols in the TP, the agreement among these data is low (Yan et al., 2015; Zhu et al., 2019). In situ observations of atmospheric aerosols are required to validate algorithms for remote sensing retrievals and constrain model simulations.

Valuable attempts on field campaigns, in addition to remote sensing and model simulations, have also been made to investigate atmospheric aerosols over the TP. Atmospheric aerosol chemical compositions together with mass loading over the TP were investigated by using filter samples collected at a few sites such as Nam Co, Qomolangma (Mt. Everest), Mt. Waliguan, Gongga, Lhasa, and Mt. Yulong (Cong et al., 2015; Kang et al., 2016; Wan et al., 2016; Xu et al., 2020; Zhang et al., 2001, 2012; Zhao et al., 2013). Chemical characterization of submicron aerosols has also been carried out by using aerosol mass spectrometer at a few sites such as Menyuan (Du et al., 2015), Mt. Yulong (Zheng et al., 2017), Nam Co (J. Xu et al., 2018), Qomolangma (Zhang, Xu, et al., 2018), and Waliguan (Zhang et al., 2019). Carbonaceous aerosol loading has been studied by online Aethalometer measurements (Cao et al., 2011; Zhang, Ming, et al., 2017) and offline filter sampling (Chen et al., 2019).

However, atmospheric aerosol physical properties and chemical compositions over the TP are still poorly quantified due to limited in situ observations. First, previous studies exhibit poor spatial representation since the studies were carried out at a few specific sites such as Nam Co, Qomolangma, and Mt. Waliguan (Zhao et al., 2019). More importantly, little is known about key aerosol parameters despite their importance in assessing aerosol radiative effects. For example, single scattering albedo (SSA) is an essential input parameter in radiative transfer model that strongly affects aerosol radiative forcing and is widely used in aerosol classification (Dubovik et al., 2002; Tian et al., 2018). Unfortunately, no field observation derived SSA (calculated from simultaneous measurements of scattering and absorption coefficients) over the TP is available in the literatures. Furthermore, deriving SSA from AERONET sunphotometer observations over the TP is not applicable due to high uncertainty under low-aerosol loading (Cong et al., 2009). Aerosol size distribution is also a key parameter that is poorly quantified in the TP. Due to a lack of aerosol size distribution, Liu et al. (2017) studied the diurnal variation of wind-blown dust aerosols at a few sites in the TP by using the mass concentration of PM<sub>2.5</sub>, which is mainly anthropogenic fine particles and not recommended for representing coarse dust aerosols.

The western TP area is considered as a potential dust emission source by previous satellite observations and model simulations (Huang et al., 2007; Xiong et al., 2016). In situ observations of atmospheric aerosols are lacking over this area due to high altitudes (higher than 4,000 m a.s.l.), remoteness, and challenging weathers. To quantify atmospheric aerosol physical properties and chemical species over the western TP, an intensive field campaign was carried out at Shiquanhe National Reference Climatological Station from July 8 to August 2, 2019. In this study, we analyzed several important characteristics of atmospheric aerosols from the data obtained during the field campaign over the site. Information of the site, data, and methodology is introduced in Section 2. Aerosol physical properties from online observations and chemical compositions from filter sampling are investigated in Sections 3 and 4, respectively. The significance of coarse mode

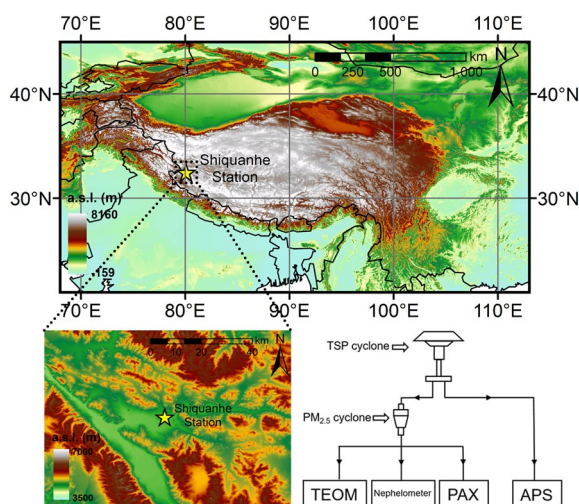


**Figure 1.** Geographical map, location of the field campaign site and airflow settings of the online instruments. The topographic data was the shuttle radar topography mission 3 (SRTM3) data from the National Aeronautics and Space Administration (NASA).

aerosols is discussed in Section 5. Summary and conclusions are presented finally in Section 6.

## 2. Observation Site, Data, and Methodology

### 2.1. A Brief Introduction to the Observation Site

The field campaign was carried out at Shiquanhe National Reference Climatological Station (32°30'N, 80°05'E, 4,278.6 m a.s.l.; “Shiquanhe station” hereafter) (Figure 1) from July 8 to August 2, 2019. The site belongs to semi-arid areas with barren land surface, strong solar radiation, long sunshine hours, and dry and cold weather. July is the warmest month (monthly average temperature of 13.8°C) and January is the coldest month (−12.7°C). The station is surrounded by Ayila Rigyu Mountains to the southwest, Gangdise Mountains to the southeast, and about 650 m to the north of the Shiquanhe River. The permanent population of Shiquanhe Town is about 24,500 and low level of anthropogenic source emissions is expected. The national highway 219, the most important highway in the western TP, is about 700 m to the west of Shiquanhe station. Therefore, there are a few vehicle source emissions around the station. There are no industrial source emissions here and the town relies only on solar and water energy to supply electricity. Electricity and natural gases are used for cooking.

The seasons in the TP has been classified as spring (pre-monsoon), summer (monsoon), autumn (post-monsoon), and winter (Chen et al., 2019; Zhao et al., 2013). In summer, the TP is controlled by both the Indian monsoon (which dominates) and the westerly winds. The TP receives more rainfall in summer due to warm moist air masses brought by the Indian monsoon, with the precipitation in southeast TP than that in west TP (Maussion et al., 2014). Shiquanhe station receives less rainfall in summer than other areas in the TP, as it is in the extreme west of the TP.

### 2.2. Description of Online Aerosol Observations

During the field observation period, a set of instruments with online observation capability from the Semi-Arid Climate and Environment Observatory of Lanzhou University (Table S1) was used to observe the physical properties of fine- and coarse-mode aerosols at Shiquanhe station, including an integrating nephelometer (model 3563, TSI Inc.) for PM<sub>2.5</sub> (particulate matter <2.5 μm in diameter) light scattering coefficient ( $b_{sca}$ ) at 450, 550, and 700 nm with a resolution of 10 s; a photoacoustic extinctions (PAX; DMT Inc.) for PM<sub>2.5</sub> light absorption and scattering coefficient ( $b_{abs}$  and  $b_{sca}$ ) at 870 nm with a resolution of 1 min; an aerodynamic particle sizer spectrometer (APS; model 3321, TSI Inc.) for the particle number size distribution in range of 542–19.81 μm (aerodynamic diameter) with a resolution of 5 min.

All online instruments were placed in a room with the temperature of about 20°C to ensure stable operations of the instruments. Ambient air and particles were sampled through a TSP (total suspended particulates) cyclone, which was about 6 m above the ground. Part of the airflow passed through a PM<sub>2.5</sub> cyclone (Model VSCC, BGI Inc.) to remove coarse-mode particles with greater than 2.5 μm in aerodynamic diameter before entering the PAX and nephelometer. The other part of the airflow entered the APS. To reflect the real state of current atmospheric aerosols, no dehumidification equipment was added. Another benefit of this measure was that the loss of particles in the transmission process could be minimized.

The observation of the online aerosol instruments was conducted between July 8 and August 2, 2019, BJT (Beijing time; BJT = UTC+8h). In addition, we acquired the meteorological data of Shiquanhe station, including temperature (T), relative humidity (RH), wind direction (WD), wind speed (WS), air pressure (P), and precipitation (Precip.). The median values of every 30 min were used in the present study to avoid the influence of extreme values in the data, so the final resolution of the data was 30 min.

### 2.3. Methodology for Online Data Analysis

SSA is a key parameter for model input and widely used in aerosols classification, which is defined in the following equation:

$$SSA = \sigma_{a,\lambda} / \sigma_{e,\lambda} = \sigma_{a,\lambda} / (\sigma_{a,\lambda} + \sigma_{s,\lambda}) \quad (1)$$

where  $\sigma_{e,\lambda}$  is aerosol extinction coefficient,  $\sigma_{a,\lambda}$  is aerosol absorption coefficient, and  $\sigma_{s,\lambda}$  is aerosol scattering coefficient at the wavelength of  $\lambda$ . The PAX observations at the wavelength of 870 nm were used in the present study.

Aerosol scattering Ångström exponent (SAE) is a widely used parameter in aerosol characterization (Cazorla et al., 2013; Zhang et al., 2020):

$$SAE = -\log(\sigma_{s,\lambda_1} / \sigma_{s,\lambda_2}) / \log(\lambda_1 / \lambda_2) \quad (2)$$

where  $\sigma_{s,\lambda}$  represents aerosol scattering coefficients at the wavelength of  $\lambda$ . In the present study,  $\lambda_1 = 450$  nm, and  $\lambda_2 = 700$  nm. As expressed in Equation 2, SAE is the wavelength dependence of aerosol scattering coefficients, with larger particles showing a smaller SAE.

### 2.4. Description of the Offline Aerosol Sampling

Medium-volume air samplers (model Laoying2030, Laoshan Electronic Instrument Factory Co.) were used to collect the TSP samples about 2 m above the ground. Aerosol samples were collected on 90 mm quartz fiber filters (model 1851-090, Whatman Inc.). Every sample was collected for 23 h from 09:00 a.m. to 08:00 a.m. of the next day at a flow rate of 100 L/min. Six blank samples were made by pumping for 1 min and then standing for 23 h in the samplers. 24 TSP samples and 6 blank samples were collected starting at 09:00 a.m. on July 8 and ending at 08:00 a.m. on August 1, 2019, BJT.

Before sampling, all quartz fiber filters were pre-baked at 550°C for 5 h to reduce the influence of absorbed organic and inorganic materials. Then, the filters were weighed using a Sartorius electronic microbalance with a sensitivity of  $\pm 0.1$  mg (model BSA124S-CW, Sartorius) after 48 h equilibration in a constant temperature and humidity environment. All samples were stored at  $-18^\circ\text{C}$  after sampling to prevent the evaporation of volatile components, and they were also placed in a constant temperature and humidity environment for 48 h before being weighed. In addition, we also collected the PM<sub>2.5</sub> and PM<sub>10</sub> samples and weighed them.

Offline TSP aerosol samples were analyzed for three types of chemical compositions: (1) water-soluble inorganic ions (WSII; i.e., Na<sup>+</sup>, K<sup>+</sup>, NH<sub>4</sub><sup>+</sup>, Ca<sup>2+</sup>, Mg<sup>2+</sup>, Cl<sup>-</sup>, NO<sub>3</sub><sup>-</sup>, and SO<sub>4</sub><sup>2-</sup>) were measured by ion chromatograph (881 Compact IC Pro, Metrohm and ICS-1500, Dionex Inc.); (2) metallic elements (i.e., Al, Ca, Mg, Fe, and Ti) were measured by inductively coupled plasma-atomic emission spectrometry (ICP-AES; iCAP 7400, Thermo); (3) organic carbon (OC) and elemental carbon (EC) were measured by DRI 2001A carbon analyzer (DRI 2001A, Atmoslytic Inc.) following the IMPROVE A protocol. The chemical analysis process is described in detail in supporting information S1.

### 2.5. Meteorological Conditions During the Observation Period

Basic meteorological elements during the observation period over Shiquanhe are shown in Figures S1 and S2. The average value  $\pm$  standard deviation of temperature, relative humidity, and wind speed during the observation period were  $13.81^\circ\text{C} \pm 4.22^\circ\text{C}$ ,  $47.01\% \pm 19.22\%$ , and  $2.71 \pm 1.31$  m s<sup>-1</sup>, respectively. The prevailing wind was from the east, followed by the one from the west. There were occasional precipitation events caused by a few thunderstorms, accounting for about 9.6% of the observation period. The average precipitation was  $1.13 \pm 1.29$  mm h<sup>-1</sup>.

Typical temperature and relative humidity diurnal variations with a peak and a bottom were recorded during the observations period (Figure 2). The temperature (relative humidity) reached the highest (lowest) between 09:00 and 10:00. The temperature (relative humidity) reached the lowest (highest) at about 18:00.

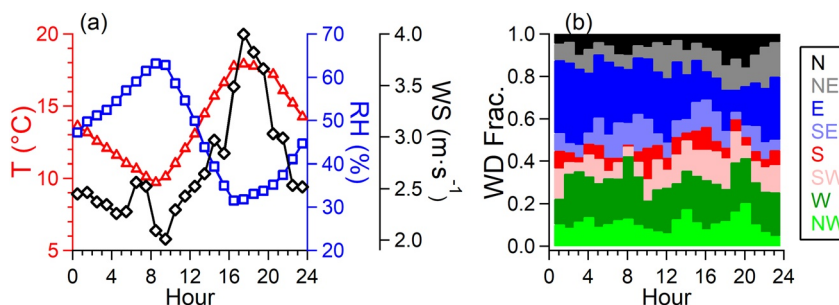


**Figure 2.** Diurnal variation of (a) temperature, relative humidity, wind speed, and (b) wind direction (Beijing time).

Wind speed varied slightly from 2.0 to 2.5 ms<sup>-1</sup> from 0:00 to 11:00, with eastern or western wind directions; then increased until 19:00 to reach a maximum value of 4.0 ms<sup>-1</sup>, with northern and western wind directions; decreased from 19:00 to 24:00, with more eastern and western wind directions.

MODIS observations during the observation period showed low aerosol loading over the TP and high aerosol loading over South Asia near the TP (supporting information S2 and Figure S3), which is consistent with long term MODIS observations during 2007–2016 (Wang et al., 2020). CALIOP observations showed that the aerosol layer over South Asia could be up to 5–6 km thick during the observation period (supporting information S2 and Figure S4). The analysis of aerosol optical properties and chemical composition in Nepal and Pakistan over a period of more than one year indicated that the aerosols in the region were significantly contributed by fossil fuel and biomass burning emissions (Chen et al., 2019). The study on carbon isotopic compositions indicates that the BC source fingerprints from the Indo-Gangetic Plain is consistent with those for the Himalayas (Li et al., 2016). Transport mechanisms of aerosols from South Asia to the TP have been studied by modeling simulations (Yang et al., 2018). About 65% of the air masses (Clusters 1, 4, and 5) were from South Asia and they did pass through the region with high AOD values as shown by MODIS observations (Figures S3 and S5). So the site was likely to be affected by aerosols from South Asia.

### 3. Atmospheric Aerosol Physical Properties

#### 3.1. Aerosol Size Distribution During Summer at Shiquanhe Station

The aerosol volume size distribution was calculated using the aerosol number size distribution from APS observations based on the spherical assumption of atmospheric particles. No persistent aerosol pollution events (natural or anthropogenic aerosol pollution events that last for multiple days) were recorded (Figure S6), though aerosol concentrations during July 13th, 24th, 25th, and 26th were higher than those of the other days. Average aerosol number concentration derived from APS was  $3.02 \pm 2.91$  N cm<sup>-3</sup> during the observation period. The aerosol number size distribution exhibited a single peak between 0.723 and

0.777 μm (Figure 3a). Fine mode aerosol (aerosols with a diameter less than 2.5 μm) number concentration accounted for  $96.00\% \pm 2.86\%$  of the total number concentration. Average aerosol volume concentration was  $8.15 \pm 8.55$  μm<sup>3</sup> cm<sup>-3</sup>. Two peaks were evident in aerosol volume size distribution (Figure 3b). The two peaks were located between 0.898–0.965 μm and 7.774–8.354 μm, respectively. Coarse mode aerosol (aerosols with a diameter larger than 2.5 μm) volume concentration accounted for  $70.58\% \pm 14.98\%$  of the total volume concentration.

The bi-modal aerosol size distributions like those in the present study have been found in some studies by remote sensing and in situ observations. Bi-modal mass size distribution was recorded using a nine-stage Anderson sampler at Ngari station (Liu et al., 2017), which is in the same region as the present study. Considering the low size resolution of the result in Liu et al. (2017), both fine and coarse mode peaks are close to those in the present study, respectively. Bi-modal volume size distribution

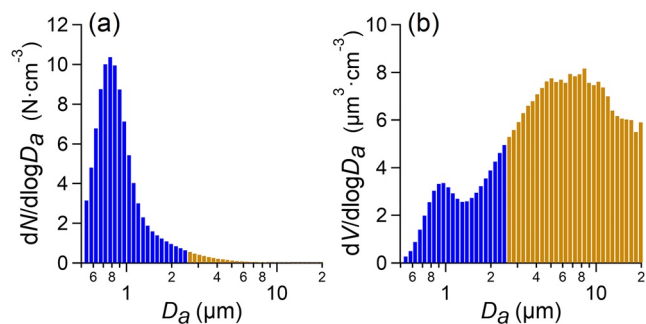


**Figure 3.** Aerosol number size distribution (a) and volume size distribution (b). Blue and brown lines represent fine mode and coarse mode aerosols, respectively.

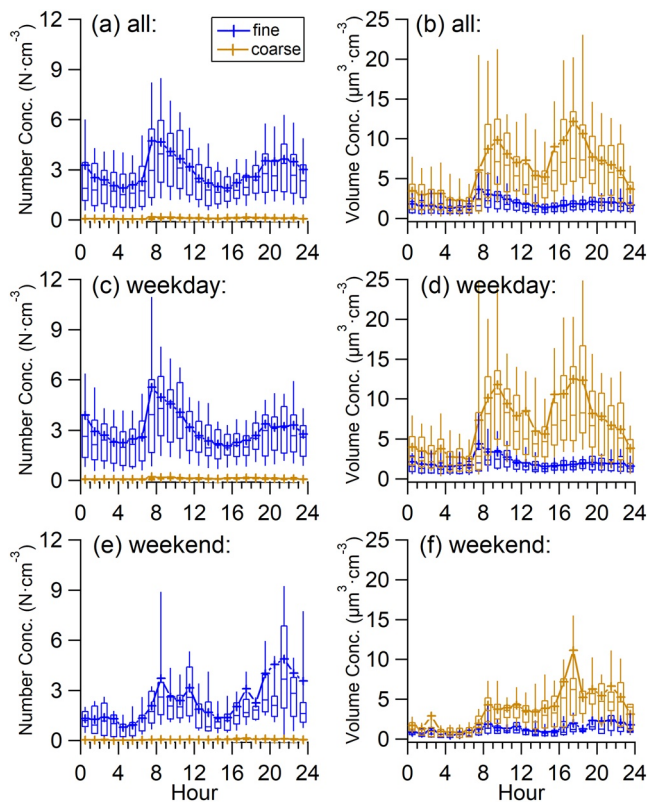


**Figure 4.** Diurnal variation of aerosol number concentration (left) and volume concentration (right) during (a and b) observation days, (c and d) weekdays, and (e and f) weekends (Beijing time). Blue and brown lines represent fine mode and coarse mode aerosols, respectively. Whiskers are 10th and 90th percentile; the top, median and bottom lines of box represent 75th, 50th, and 25th percentile respectively; the plus signs are the averaged values.

was also evident from AERONET sunphotometer measurements at Muztagh Ata site (Zhu et al., 2019), which is also in west TP. The measurements in Zhu et al. (2019) was for the total column of the atmosphere while those in the present study was at the ground, so there is no point to compare fine and coarse mode peaks between them. Similar bi-modal aerosol size distributions in the present study have also been observed at dust source areas (Parajuli et al., 2019; Sow et al., 2009), indicating the more dust emissions than anthropogenic pollutants in west TP. However, we can only briefly compare the results of these studies (e.g., how many peaks are present) because there are large systematic differences between aerosol size distributions obtained by different methods, such as single particle method, aerodynamic method, method based on optical particle counters, and optical inversion method (Müller et al., 2012; Reid et al., 2003). Thus, we further compare the results in the present study with other studies using APS (e.g., location and width of peaks). The aerosol size of the fine mode peak in the present study was larger than that in urban areas (Yu et al., 2017), which was attributed to coarser MD aerosols in this size range. The aging of fine mode aerosols may also contribute to larger size in the fine mode, which requires further investigations. The location and width of the coarse mode peak in the present study were like those at dust sources areas (Parajuli et al., 2016; Reid et al., 2003; Sow et al., 2009), indicating local emissions of dust aerosol at Shiquanhe station in the coarse mode size range. The coarse mode volume concentration in the present study was higher than that at Mt. Yulong station (a southeastern TP site) in March and April (Shang et al., 2018). The coarse mode peak at Mt. Yulong station in March and April is at  $\sim 2.6 \mu\text{m}$  (modified to aerodynamic diameter from stokes diameter), which is smaller than that at Shiquanhe station in July. The reason for this difference might be that Mt. Yulong station was dominated by long-transported dust aerosol in March and April.

Overall, the bi-modal size distribution of atmospheric aerosols was observed using APS instrument located at Shiquanhe station. Moreover, coarse mode aerosols make up a large portion of aerosol volume concentrations (Figure 3b), which is further illustrated by filter sampled mass concentrations of  $\text{PM}_{10}$  and TSP in Section 6.

Diurnal variation of aerosol number and volume concentrations was studied to reveal more details of atmospheric aerosols at Shiquanhe station. Two peaks in the morning and afternoon are evident in aerosol concentration plots, and aerosol concentrations (both fine and coarse modes) showed large differences between weekdays and weekends (Figure 4). The peaks of both fine and coarse modes in the morning on weekdays were more than doubled to those on weekends, indicating a significant effect of anthropogenic activities on fine and coarse mode aerosols in the morning. The peak of coarse mode aerosol volume concentration at about 18:00 was still present on weekends, even though the coarse mode aerosol volume concentration in the afternoon was much lower. It could be attributed to wind-blown dust due to high wind speed or changes in wind direction (Figure 2). Fine mode aerosol number concentrations reached another peak at about 21:00–22:00 and were higher on weekends, which might also be caused by more human activities (e.g., cooking) on weekends. It is interesting to note that though the coarse mode number concentration was relatively low, the volume concentration of coarse mode aerosol was higher than that of fine mode aerosol. Since aerosol volume concentration is related to optical parameters, coarse mode aerosols might significantly contribute to radiative budget over western TP in summer.

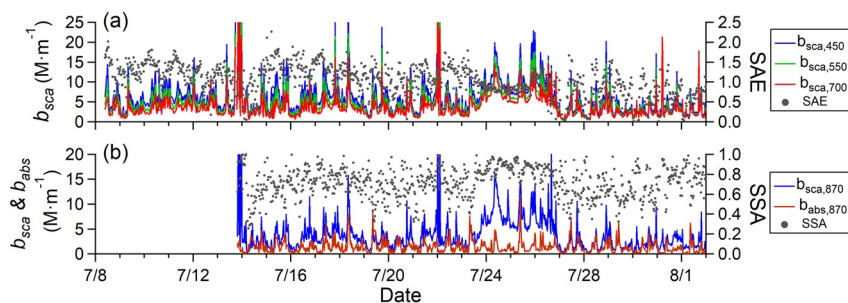


**Figure 5.** Temporal variation of (a) aerosol scattering coefficients at 450, 550, and 700 nm and scattering Ångström exponent (SAE); (b) aerosol scattering coefficients, absorption coefficients, and single scattering albedo (SSA) at 870 nm (Beijing time).

### 3.2. Aerosol Optical Properties During Summer at Shiquanhe Station

Ambient aerosol scattering coefficients, absorption coefficients and size distribution were observed by using online instruments at Shiquanhe station. Atmospheric aerosols showed relatively large fluctuation during the observation period (Figure 5). During the observation period, the average  $PM_{2.5}$  scattering coefficients at 450, 550, 700, and 870 nm were  $6.09 \pm 5.36$ ,  $4.79 \pm 4.31$ ,  $3.83 \pm 3.34$ , and  $3.80 \pm 3.64 M m^{-1}$ , respectively; the average  $PM_{2.5}$  absorption coefficient at 870 nm were  $1.39 \pm 1.26 M m^{-1}$ .

The average SSA of  $PM_{2.5}$  derived from the observations of PAX was  $0.73 \pm 0.18$ , which is significantly lower than expected. Note that SSA is wavelength dependent and the results of SSA in the present study was calculated by using scattering and absorption coefficients of  $PM_{2.5}$  at the wavelength of 870 nm. The average SSA of  $PM_{2.5}$  at 870 nm was 0.87 during wintertime at a coastal city of Xiamen, China (Deng et al., 2016) and 0.78 from mid-August to mid-October at a megacity of Xi'an, China (Zhu et al., 2015). The relatively low value of 0.78 during autumn at Xi'an was attributed to significant light absorption by BC aerosols (Zhu et al., 2015). The measurements of PAX also showed very low values of SSA at 870 nm for laboratory-simulated western US wildfires (Selimovic et al., 2018). Generally, SSA values of higher than 0.85 for urban pollution aerosols and lower than 0.80 for high absorbing aerosols are expected at 870 nm (Deng et al., 2016; Retama et al., 2015; Zhu et al., 2015). The unexpected low value of SSA indicates strong absorption of the fine mode atmospheric aerosols at Shiquanhe station. SSA is a key input parameter for numerical models to assess aerosols radiative effects. Aerosol radiative efficiency is strongly dependent on SSA (Tian et al., 2018) and a small change in SSA leads to significant variation in radiative effects (Haywood & Boucher, 2000). Thus, aerosol absorption might be underestimated in previous studies on the assessment of aerosol effects in summer over the west TP. To better understand the temporal variation of SSA during the observation period (Figure 5b), we compared the mass concentrations of chemical compositions between samples with  $SSA < 0.70$  and  $SSA > 0.70$ . The secondary inorganic compositions (e.g.,  $SO_4^{2-}$ , and  $NH_4^+$ ) and the MD compositions (e.g., Al, Ca) for the samples with  $SSA > 0.70$  were higher than those with  $SSA < 0.70$  (Figure S8), leading to relatively high scattering and low absorbing for the samples with  $SSA > 0.70$ .

The spectral dependence of aerosol scattering coefficients was studied by combing observations from a nephelometer and a PAX. Aerosol scattering coefficients decreased exponentially with wavelength, with an average SAE of  $1.04 \pm 0.42$  (Figure 6a). Note that SAE in the present study was derived from scattering coefficients of  $PM_{2.5}$ . The SAE is related to the average particle size of aerosols, which is widely used in aerosol characterizing and classification. Some studies have also calculated SAE using aerosol scattering coefficients. The SAE was  $0.52 \pm 0.31$  for Gobi Desert aerosols and negative values for aerosols during dust storms in northwest China (Wang et al., 2018) while  $1.8 \pm 0.3$  in an urban environment (Lyamani et al., 2008). Study in a rural environment near the mega-city Guangzhou, China suggested higher value of the parameter during smoky period ( $1.50 \pm 0.24$ ) than nonsmoky period ( $1.46 \pm 0.21$ ) (Garland et al., 2008). The SAE calculated using scattering coefficients at 450 and 700 nm was  $1.04 \pm 0.42$  at Shiquanhe station.

Aerosol scattering coefficients at 450, 550, 700, and 870 nm showed similar diurnal variation (Figures 6b and 6c): two evident peaks at about 09:00 and between 21:00 and 22:00. The time aerosol

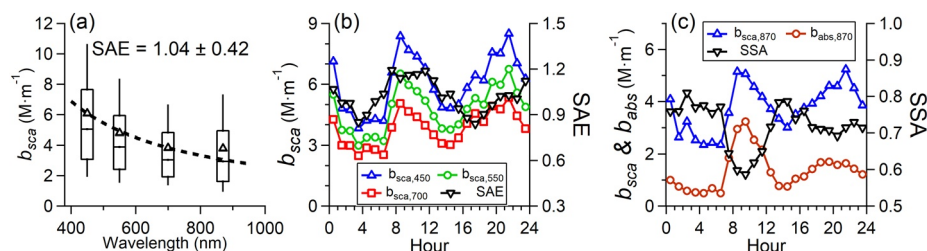


**Figure 6.** (a) Spectral dependence of aerosol scattering coefficient derived from nephelometer and PAX. Whiskers are 10th and 90th percentile; the top, median and bottom lines of box represent 75th, 50th and 25th percentile respectively; the plus signs are the averaged value. Diurnal variation of (b) aerosol scattering coefficients at 450, 550, and 700 nm and scattering Ångström exponent (SAE); (c) aerosol scattering coefficients, absorption coefficients, and single scattering albedo (SSA) at 870 nm (Beijing time).

scattering coefficients reached the peaks was in accordance with that of the fine mode aerosol number concentrations (Figure 4a). SAE reached the minimum value of 0.84 at 04:00, then started to increase and remained at about 1.2 until 12:00. The SAE started to decrease again and reached a low value of 0.84 at 18:00, then began to increase after 18:00. Low value of SAE in the afternoon indicated aerosol size growth caused by wind blowing dust aerosols during that time. Diurnal variation of absorption coefficients seemed to be caused by anthropogenic activities with one pronounced peak at 09:00 and a slight peak at 21:00. The significantly enhanced absorption led to minimum SSA in the morning, despite the increase in scattering. The minimum value of average SSA at 870 nm was even lower than 0.60 (Figure 6c), indicating strong absorbing fine mode aerosols induced by anthropogenic activities in the morning.

## 4. Atmospheric Aerosol Chemical Compositions

### 4.1. Mass Concentration of OC and EC

During the observation period, the average mass concentrations of OC and EC were  $1.56 \pm 0.43$  and  $0.09 \pm 0.11 \mu\text{g m}^{-3}$ , respectively (Table S2). OC dominated the mass concentration of carbonaceous aerosols, which accounted for 94.6% of TC (total carbon;  $\text{TC} = \text{OC} + \text{EC}$ ) (Figure 7). The ratio of OC to EC varies for aerosols of different combustion sources, 0.3 to 7.6 for coal burning emissions, 0.7 to 2.4 for vehicle emissions, and 4.1 to 14.5 for biomass burning emissions (Watson et al., 2001). The OC/EC ratios were generally

below 10 in the TP (Chen et al., 2019; Zhang, Cao, et al., 2018). However, the OC/EC ratio in the present study was 17.4, suggesting that biomass burning emissions might contribute more than fossil fuel burning emissions around Shiquanhe station. Aging of aerosols is another possible reason that leads to high OC/EC ratios (Zhang et al., 2019). According to the backward trajectories (Figure S5), it was likely to be the influence of aerosols transported from South Asia (Wang et al., 2019).

The correlation coefficients between aerosol chemical species were investigated to better understand the origins of aerosol species (Table 1).  $\text{K}^+$  is a tracer of biomass burning emissions (Zhang, Cao, et al., 2018). EC showed almost no linear correlation ( $R^2 = 0.01$ ) with  $\text{K}^+$  while the correlation coefficient of OC and  $\text{K}^+$  was higher ( $R^2 = 0.27$ ), suggesting that more OC was originated from biomass burning than EC. This also explained the low correlation coefficient between OC and EC ( $R^2 = 0.14$ ). In addition, OC exhibited a good relationship with metallic elements (i.e., Al, Ca, Mg, Fe, and Ti) while EC showed little dependence on metallic elements, which was attributed to the decomposition of carbonate (i.e.,  $\text{CaCO}_3$  and  $\text{MgCO}_3$ ) at high temperature while measuring OC and EC (Chen et al., 2019).

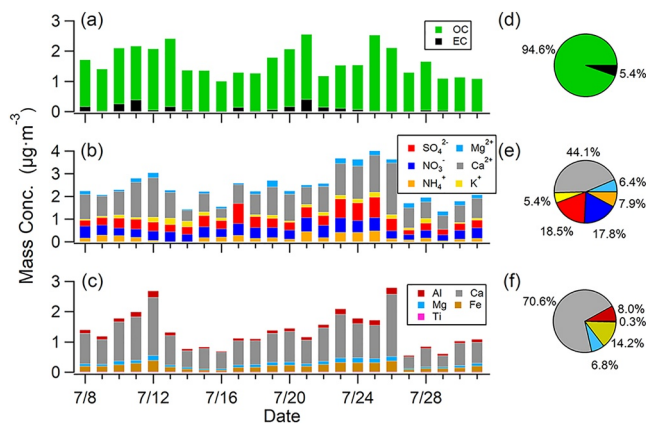


**Figure 7.** The time series of mass concentrations of (a) OC, EC, (b) WSII, and (c) metallic elements and (d, e, and f) their relative mass contributions.

**Table 1**  
Correlation Matrix of Aerosol Chemical Species and Meteorological Parameters

	OC	EC	NH <sub>4</sub> <sup>+</sup>	K <sup>+</sup>	SO <sub>4</sub> <sup>2-</sup>	NO <sub>3</sub> <sup>-</sup>	Ca <sup>2+</sup>	Mg <sup>2+</sup>	Al	Ca	Mg	Fe	Ti	T	RH	WS
OC	1.00	0.14	0.06	0.27	0.05	0.03	0.38	0.02	0.34	0.30	0.21	0.30	0.23	0.07	-0.12	0.00
EC		1.00	0.08	-0.01	0.00	0.06	0.01	-0.03	0.03	0.05	0.02	0.05	0.12	0.01	-0.06	0.02
NH <sub>4</sub> <sup>+</sup>			1.00	-0.00	0.56	0.48	0.04	0.02	0.11	0.03	0.19	0.12	0.04	0.05	-0.29	0.03
K <sup>+</sup>				1.00	0.02	0.01	0.11	0.01	0.10	0.11	0.08	0.07	0.05	-0.01	0.00	-0.03
SO <sub>4</sub> <sup>2-</sup>					1.00	0.40	0.16	0.04	0.20	0.13	0.32	0.21	0.06	0.00	-0.21	0.12
NO <sub>3</sub> <sup>-</sup>						1.00	0.03	0.01	0.09	0.04	0.17	0.12	0.09	-0.00	-0.10	0.02
Ca <sup>2+</sup>							1.00	0.24	0.84	0.82	0.67	0.81	0.56	0.18	-0.29	0.38
Mg <sup>2+</sup>								1.00	0.19	0.08	0.26	0.22	0.04	0.25	-0.29	0.08
Al									1.00	0.83	0.82	0.94	0.75	0.27	-0.42	0.46
Ca										1.00	0.71	0.82	0.76	0.11	-0.21	0.44
Mg											1.00	0.91	0.63	0.20	-0.48	0.43
Fe												1.00	0.76	0.27	-0.48	0.49
Ti													1.00	0.31	-0.38	0.46
T														1.00	-0.71	0.22
RH															1.00	-0.35
WS																1.00

Note: The plus or minus of the correlation coefficient indicates the plus or minus of the slope.

#### 4.2. Mass Concentration of Water-Soluble Inorganic Ions (WSII)

The average mass concentrations of K<sup>+</sup>, NH<sub>4</sub><sup>+</sup>, SO<sub>4</sub><sup>2-</sup>, NO<sub>3</sub><sup>-</sup>, Ca<sup>2+</sup>, and Mg<sup>2+</sup> were 0.13 ± 0.07, 0.19 ± 0.13, 0.45 ± 0.20, 0.43 ± 0.11, 1.07 ± 0.43, and 0.16 ± 0.07 μg m<sup>-3</sup>, respectively (Table S2). Na<sup>+</sup> and Cl<sup>-</sup> were not included in the present study because the Na<sup>+</sup> concentration was greatly influenced by quartz fiber filters and glass containers and the Cl<sup>-</sup> concentration too low to be detected. The average mass concentration of WSII (the sum of NH<sub>4</sub><sup>+</sup>, K<sup>+</sup>, Ca<sup>2+</sup>, Mg<sup>2+</sup>, SO<sub>4</sub><sup>2-</sup>, and NO<sub>3</sub><sup>-</sup>) was 2.43 ± 0.73 μg m<sup>-3</sup>. Ca<sup>2+</sup> and Mg<sup>2+</sup> contributed about 50% of WSII (Figure 7), indicating high contribution of MD aerosols at Shiquanhe station.

Ca<sup>2+</sup> might be originated from wind-blown dust due to a high positive correlation between Ca<sup>2+</sup> and wind speed (Table 1). The K<sup>+</sup> concentration at Shiquanhe station was much higher than those in the central (0.01 ± 0.01 μg m<sup>-3</sup>), southeast (0.04 ± 0.03 μg m<sup>-3</sup>), and northeast TP (0.01 μg m<sup>-3</sup>) (Xu et al., 2015; Zhao et al., 2013; Zhang, Xu, et al., 2017), indicating more biomass burning aerosols were present in the western TP than in other regions in summer. Negative correlations were found between secondary inorganic species (i.e., NH<sub>4</sub><sup>+</sup>, SO<sub>4</sub><sup>2-</sup>, and NO<sub>3</sub><sup>-</sup>) and relative humidity, inferring the removal of these species by wet deposition at Shiquanhe station. The secondary inorganic species also exhibited good correlations with each other, suggesting that they came from the same pollutant source.

The ionic balance of WSII is illustrated in Figure 8. The slope of linear fitting between cations and anions was 2.77 and the correlation was poor (R<sup>2</sup> = 0.29) (Figure 8a). The ionic balance was effectively improved with the correlation coefficient increased to 0.65 and the slope decreased to 1.13 when Ca<sup>2+</sup> and Mg<sup>2+</sup> were excluded from the cations. The reason for this phenomenon was the participation of CO<sub>3</sub><sup>2-</sup> and/or HCO<sub>3</sub><sup>-</sup> (Wan et al., 2016). Generally, carbonates in MD, such as CaCO<sub>3</sub> and MgCO<sub>3</sub>, dissolve in water to produce CO<sub>3</sub><sup>2-</sup> and/or HCO<sub>3</sub><sup>-</sup>, but their solubility is extremely low. The influence of trace amounts of CO<sub>3</sub><sup>2-</sup> and/or HCO<sub>3</sub><sup>-</sup> is limited when aerosol concentrations are high. But for the TP where aerosol loading is low, the influence of CO<sub>3</sub><sup>2-</sup> and/or HCO<sub>3</sub><sup>-</sup> becomes

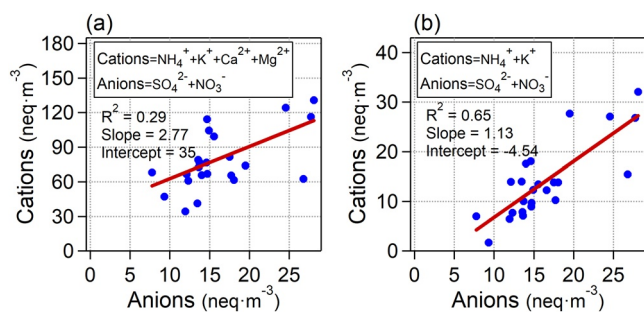


**Figure 8.** (a) Ionic balance; (b) Ionic balance, excluding Ca<sup>2+</sup> and Mg<sup>2+</sup>. Concentrations are reported in nanogram-equivalent weight per cubic meter (neq·m<sup>-3</sup>).

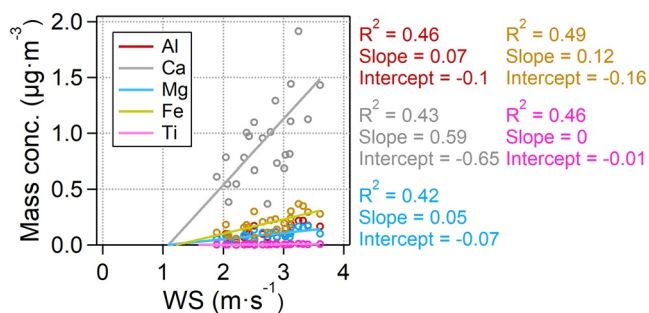


**Figure 9.** The relationship between mass concentrations of metallic elements and wind speed.

important. In addition, the fitting slope was still higher than one even without considering  $\text{Ca}^{2+}$  and  $\text{Mg}^{2+}$ , which might be due to the presence of a small amount of  $\text{NH}_4^+$  and  $\text{K}^+$  in the form of carbonate, or the influence of organic acid.

### 4.3. Mass Concentration of Metallic Elements

The average mass concentrations of Al, Ca, Mg, Fe, and Ti were  $0.11 \pm 0.05$ ,  $0.96 \pm 0.43$ ,  $0.09 \pm 0.04$ ,  $0.19 \pm 0.09$ , and  $0.005 \pm 0.003 \mu\text{g m}^{-3}$ , respectively (Table S2). Ca accounted for the most metallic elements mass (70.6%), followed by Fe (14.2%), Al (8.0%), Mg (6.8%), and Ti (0.3%) (Figure 7). The elemental Al, Ca, Mg, Fe, and Ti are better tracers of MD aerosols than the ionic  $\text{Ca}^{2+}$  and  $\text{Mg}^{2+}$ , since  $\text{Ca}^{2+}$  and  $\text{Mg}^{2+}$  represent only the water-soluble fraction of MDs.

Al, Ca, Mg, Fe, and Ti exhibited excellent correlations with each other (Table 1), indicating that they originated from the same source. The correlation coefficients between metallic elements and wind speed were much higher than those between nondust components and wind speed, and the slopes of the fitting lines were higher than zero (Figure 9 and Table 1). All the metallic elements started to increase with wind speed when wind speed was higher than  $1.0 \text{ m s}^{-1}$ . These findings indicated that MD aerosols at Shiquanhe station were generated locally by strong winds during the observation period. In addition, Al, Ca, Mg, Fe, Ti,  $\text{Ca}^{2+}$ , and  $\text{Mg}^{2+}$  positively correlated with temperature, and negatively correlated with relative humidity. A possible reason is that high temperature and low-relative humidity lead to a reduction in the threshold of dust burst under barren conditions.

### 4.4. Mass Closure of Offline Aerosol Samples

Organic matter (OM), EC, MD, and nondust water-soluble inorganic ions (nd-WSII) were used to reconstruct the mass closure of offline aerosol samples. The ratio of OM to OC mass, referred to as OM/OC, is required to calculate OM mass concentration (Guinot et al., 2007; Turpin & Lim, 2001). Turpin and Lim (2001) proposed the OM/OC values of  $1.6 \pm 0.2$  for urban aerosols,  $2.1 \pm 0.2$  for nonurban aerosols, and  $2.4 \pm 0.2$  for aerosols from biomass burning areas, which is widely used across the world (Sciare et al., 2005; Xing et al., 2013; Zhao et al., 2013). The measured OM/OC values in the TP vary from 2.28 to 2.63 for different regions and seasons (J. Xu et al., 2018; Zhang et al., 2019; Zheng et al., 2017) and the OM/OC values generally were lower in summer. The OM/OC value of 2.28 was used in the present study to calculate OM mass.

MD mass was simply derived from one single metallic element mass with a weighting factor (e.g., Al/0.07 and Fe/0.04) in some studies (Sciare et al., 2005; Zhao et al., 2013). However, the proportions of metallic elements in MD vary greatly for different regions and particle sizes (Kang et al., 2016; Wang et al., 2016; Zhang et al., 2003). Thus, the MD mass calculation by a single metallic element suffers from large uncertainty. Multiple metal and nonmetallic elements were used in previous studies to calculate MD mass more accurately (Malm et al., 1994; Marcazzan et al., 2001). For example, the MD mass can be calculated as follows:

$$\begin{aligned} \text{Mineral dust} &= 1.15 \cdot \left( \frac{M_{r,\text{Al}_2\text{O}_3}}{A_{r,\text{Al}}} \cdot [\text{Al}] + \frac{M_{r,\text{SiO}_2}}{A_{r,\text{Si}}} \cdot [\text{Si}] + \frac{M_{r,\text{TiO}_2}}{A_{r,\text{Ti}}} \cdot [\text{Ti}] + \frac{M_{r,\text{Fe}_x\text{O}_y}}{A_{r,\text{Fe}}} \cdot [\text{Fe}] \right. \\ &\quad \left. + \frac{M_{r,\text{K}_2\text{O}}}{A_{r,\text{K}}} \cdot [\text{K}] + \frac{M_{r,\text{CaO}}}{A_{r,\text{Ca}}} \cdot [\text{Ca}] \right) \quad (3) \\ &= 1.15 \cdot \left( 1.89 \cdot [\text{Al}] + 2.14 \cdot [\text{Si}] + 1.67 \cdot [\text{Ti}] + 1.36 \cdot [\text{Fe}] + 1.2 \cdot [\text{K}] + 1.4 \cdot [\text{Ca}] \right) \end{aligned}$$

where  $M_{r,n}$  refers to the relative molecular mass of oxide  $n$ ,  $A_{r,m}$  refers to the relative atomic mass of element  $m$ ; the  $M_{r,n}$  of Fe oxides was obtained on the premise that FeO and  $\text{Fe}_2\text{O}_3$  accounted for half of the molality of Fe oxides respectively. Since Si was not measured, [Si] was replaced by  $[\text{Si}] = 4[\text{Al}]$  (Wang et al., 2016);

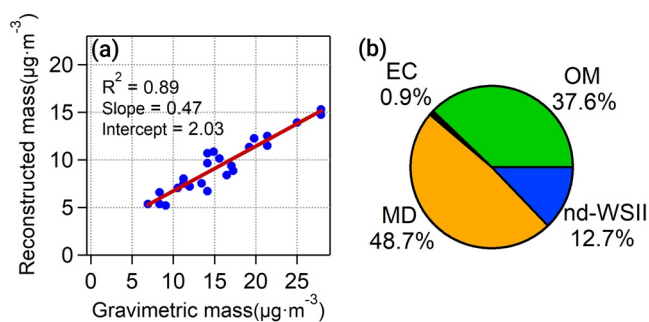


**Figure 10.** (a) The relationship between reconstructed mass concentration and gravimetric mass concentration; (b) the relative contributions of organic matter (OM), elemental carbon (EC), nondust water-soluble inorganic ions (nd-WSII), and mineral dust (MD) to the reconstructed mass concentration.

Since  $K$  was not measured,  $[K]$  was replaced by  $[K] = 0.6[Fe]$  (Malm et al., 1994). Multiply by 1.15 to compensate for the mass of the other metallic oxides not measured.

It was assumed that the Ca and Mg elements existed in the form of metallic oxides (i.e., CaO and MgO) in Equation 3. However, Ca and Mg elements can also exist in the form of carbonate (i.e.,  $\text{CaCO}_3$  and  $\text{MgCO}_3$ ). Some rocks may indeed contain CaO and MgO, such as basalt and tuff, but CaO and MgO are generally much less than other metallic oxides. Even small amounts of CaO and MgO in MD are easily oxidized to form  $\text{CaCO}_3$  and  $\text{MgCO}_3$  by atmospheric  $\text{CO}_2$  because of the larger reaction interface of MD than that of rocks. Therefore, it is better to assume that the Ca and Mg elements in MD are all in the form of carbonate. The ionic balance in aqueous solution also proved the existence of carbonate (Section 4.2). Equation 3 was revised based on the above discussions:

$$\begin{aligned} \text{Mineral dust} &= 1.15 \cdot \left( \frac{M_{r,\text{Al}_2\text{O}_3}}{A_{r,\text{Al}}} \cdot [\text{Al}] + \frac{M_{r,\text{SiO}_2}}{A_{r,\text{Si}}} \cdot [\text{Si}] + \frac{M_{r,\text{TiO}_2}}{A_{r,\text{Ti}}} \cdot [\text{Ti}] + \frac{M_{r,\text{Fe}_x\text{O}_y}}{A_{r,\text{Fe}}} \cdot [\text{Fe}] \right. \\ &\quad \left. + \frac{M_{r,\text{K}_2\text{O}}}{A_{r,\text{K}}} \cdot [\text{K}] + \frac{M_{r,\text{CaO}}}{A_{r,\text{Ca}}} \cdot [\text{Ca}] \right) \\ &\quad + \frac{M_{r,\text{CaCO}_3} - M_{r,\text{CaO}}}{A_{r,\text{Ca}}} \cdot [\text{Ca}] + \frac{M_{r,\text{MgCO}_3} - M_{r,\text{MgO}}}{A_{r,\text{Mg}}} \cdot [\text{Mg}] \\ &= 1.15 \cdot (1.89 \cdot [\text{Al}] + 2.14 \cdot [\text{Si}] + 1.67 \cdot [\text{Ti}] + 1.36 \cdot [\text{Fe}] + 1.2 \cdot [\text{K}] \\ &\quad + 1.4 \cdot [\text{Ca}] + 1.1 \cdot [\text{Ca}] + 1.83 \cdot [\text{Mg}]) \end{aligned} \quad (4)$$

The new formula considered the heavier mass of  $\text{CaCO}_3$  and  $\text{MgCO}_3$  than that of CaO and MgO. The old Equation 3 would result in the underestimation of MD mass, which was about 26.7% in the present study. Of course, there were still several possible error sources: (1) the Ca and Mg elements might also exist in the forms of sulfate and nitrate, but it could be judged from the correlation coefficients and ionic balance that Ca and Mg in those forms were low (Figure 8 and Table 1); (2) the accuracy of calculations for Si, Fe, and K; (3) the accuracy of the compensation coefficient of 1.15.

Since  $\text{Ca}^{2+}$  and  $\text{Mg}^{2+}$  originated from the water-soluble fraction of MD, they were excluded when calculating the mass closure. The sum of  $\text{SO}_4^{2-}$ ,  $\text{NO}_3^-$ ,  $\text{NH}_4^+$ , and  $\text{K}^+$  was defined as the nd-WSII.

The reconstructed mass concentration was reasonable because it correlated well with gravimetric mass concentration ( $R^2 = 0.89$ ) (Figure 10). However, the slope of the fitting line was only 0.47, which might be due to the water vapor absorbed by filters and/or the losses of chemical compositions during extraction. The intercept of the fitting line was not close to zero, possibly because of the overestimation of carbonaceous aerosols due to carbonate decomposition. In addition, Equation 4 did improve the results, as the correlation was increased using Equation 4 compared to using Equation 3 (Figure S9). The reconstruction mass concentrations of OM, EC, MD, and nd-WSII were  $3.55 \pm 0.98$ ,  $0.09 \pm 0.11$ ,  $4.61 \pm 1.58$ , and  $1.20 \pm 0.41 \mu\text{g}\cdot\text{m}^{-3}$ , respectively. The MD contributed the most (48.7%) and the EC contributed the least (0.9%). The MD and EC were two important absorptive aerosols in the atmosphere (Tian et al., 2018). The radiative forcing caused by the absorption of MD was possibly higher than that of EC because the MD mass was tens of times higher than the EC (or BC) mass (Figure 10), although the mass absorption cross section of EC was higher than that of MD.

## 5. Discussions on the Significance of Coarse Mode Aerosols

Daily PM concentrations were also obtained from the filter samples, with monthly average  $\text{PM}_{2.5}$ ,  $\text{PM}_{10}$ , and TSP of  $5.18 \pm 1.49$ ,  $8.64 \pm 2.60$ , and  $15.71 \pm 5.92 \mu\text{g}\cdot\text{m}^{-3}$ , respectively (Figures 11a). The ratios of  $\text{PM}_{2.5}$  to  $\text{PM}_{10}$  and  $\text{PM}_{2.5}$  to TSP were 0.60 and 0.33, respectively. The ratios of  $\text{PM}_{2.5}$  to TSP at two sites in megacity

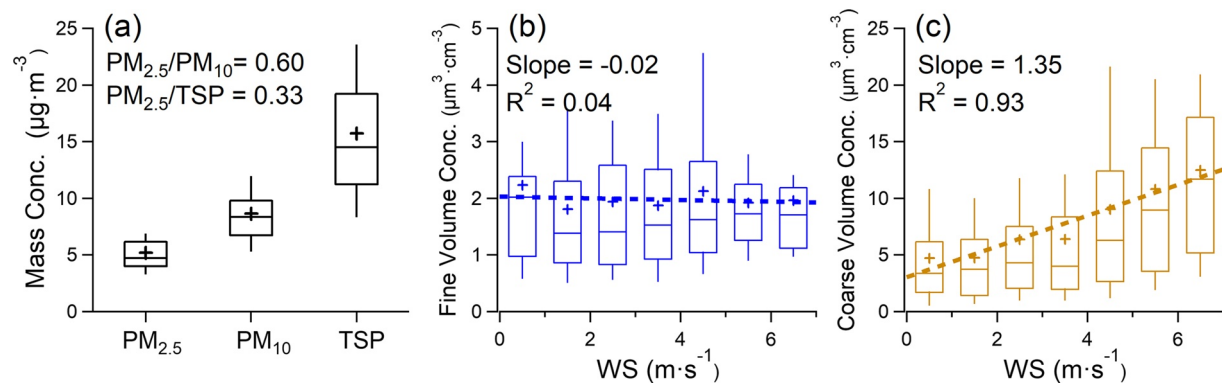


**Figure 11.** (a) The gravimetric mass concentrations of  $PM_{2.5}$ ,  $PM_{10}$ , and TSP derived from filter samples. Dependence of (b) fine and (c) coarse mode aerosol volume concentrations on wind speed. Whiskers are 10th and 90th percentile; the top, median, and bottom lines of box represent 75th, 50th, and 25th percentile, respectively; the plus signs are the average value.

Nanning, China were 0.61 and 0.50 (Hu et al., 2012), much higher than that at Shiquanhe station. The ratio of  $PM_{2.5}$  to TSP was 0.51 (calculated from the average mass concentrations of  $PM_{2.5}$  and TSP of 21.27 and  $41.47 \mu\text{g m}^{-3}$ , respectively) at a northeastern TP site (Zhang et al., 2014). Such low ratio of  $PM_{2.5}$  to TSP in the present study indicates the significance of coarse mode MD aerosols at Shiquanhe station.

The above analysis on aerosol physical properties and chemical compositions shows the importance of coarse mode MD aerosols over Shiquanhe. However, no dust events were recorded during the observation period based on weather records from Shiquanhe station. In addition, coarse mode aerosols showed specific diurnal variation (Figure 4), and metallic elements exhibited excellent correlations with wind speed (Figure 9). So, it is safe to conclude that coarse mode MD aerosols at Shiquanhe station during the observation period were from local emissions, rather than transported from dust source regions by atmospheric circulation.

Local dust emission is controlled by wind speed at a given environment (Kandler et al., 2009; Shao, 2008). So, the relationship between aerosol volume concentration and wind speed was studied (Figures 11b and 11c). Fine mode aerosol concentration showed little dependence on wind speed ( $R^2 = 0.04$ ). However, strong positive correlation was found between coarse mode aerosol concentration and wind speed ( $R^2 = 0.93$ ), which was consistent with the result in Figure 9, demonstrating the importance of local dust emissions. Considering the significant differences of coarse mode aerosols between weekdays and weekends in the morning (Figures 4d and 4f), local dust emissions at Shiquanhe station in summer were the result of a combination of anthropogenic activities and meteorological conditions.

## 6. Summary and Conclusions

The assessment of atmospheric aerosol radiative effects suffers from large uncertainties over the TP region due to limited observations. The key aerosol parameters such as SSA and volume size distributions were quantified for the first time in the western TP based on intensive in situ observations at Shiquanhe station from July 8 to August 2, 2019. The main conclusions are summarized below:

- (1) Fine mode aerosols showed unexpected low monthly average SSA value of  $0.73 \pm 0.15$  at Shiquanhe station. The minimum value of the diurnal SSA was even lower than 0.6 in the morning. Such low values of SSA indicates strong absorption of the fine mode anthropogenic aerosols over the western TP.
- (2) Bi-modal size distribution was captured by the volume concentrations derived from the APS observations, with the fine mode one located between 0.898 to  $0.965 \mu\text{m}$  and the coarse mode one between 7.774 and  $8.354 \mu\text{m}$ . The ratio of filter sampled  $PM_{2.5}$  to TSP reached a high value of 0.33. It is safe to conclude that coarse mode MD particles dominate the atmospheric aerosols over the western TP.
- (3) Chemical compositions in TSP showed the contributions of MD, OM, nd-WSII, and EC were 48.7%, 37.6%, 12.7%, and 0.9%, respectively. The contribution of MD was tens of times greater than that of EC.

MD were mainly composed of carbonates and might have a significant impact on the determination of OC and EC. There were positive correlations between wind speed and metallic elements in MD. The high  $K^+$  concentration and high OC/EC value indicated that the influence of biomass burning was stronger than that of fossil fuel burning at Shiquanhe station.

- (4) Coarse mode MD aerosols at Shiquanhe station during the observation time were from local emissions, rather than transported from dust source regions by atmospheric circulation. Fine mode aerosol concentration showed little dependence on wind speed while strong positive correlation was found between coarse mode aerosol concentration and wind speed, indicating the importance of wind-blown dust particles at Shiquanhe station.

The present study not only quantified physical properties and chemical compositions of atmospheric aerosols in the western TP, but also highlight the effects of anthropogenic activities on fine aerosols and wind speed on coarse dust aerosols and their importance for aerosol radiative forcing in the TP. Unexpected high absorption of fine anthropogenic aerosols (very low SSA) and high mass fraction of MD aerosols were found. Given very pristine condition in the TP, it should be kept in mind that aerosol absorption works together with aerosol loading in modulating aerosol radiative effects. In addition, the unexpected high absorption may also affect the snow and ice cover because the deposition of absorbing aerosols (e.g., BC and MD) on snow and ice cover might lead to a lowered surface albedo and the melting of snow and ice (Kang et al., 2019). Our results suggest the need to carefully consider the radiative effects caused by aerosol absorption in the TP region.

### Data Availability Statement

The original aerosol observation data of the Shiquanhe station are available at the National Tibetan Plateau Data Center (<http://data.tpdac.ac.cn/zh-hans/data/26316216-148b-4c07-84dd-fad1ebb25b58/>, <http://data.tpdac.ac.cn/zh-hans/data/27465192-6dc7-4986-8abe-bb73febc795d/>, <http://data.tpdac.ac.cn/zh-hans/data/47d-4fee1-29aa-4404-a482-bf7d49e34310/>, <http://data.tpdac.ac.cn/zh-hans/data/6e6fd4fd-6e41-4e2d-b9d8-efa-2ceb0bfa/>, <http://data.tpdac.ac.cn/zh-hans/data/d37ceb67-e347-4aa0-8f02-1879c987b7eb/>).

### Acknowledgments

This research was supported by the Second Tibetan Plateau Scientific Expedition and Research Program (STEP, Grant No. 2019QZKK0602), Gansu Provincial Special Fund Project for Guiding Scientific and Technological Innovation and Development (2019ZX-06), and the Fundamental Research Funds for the Central Universities (lzujbky-2020-kb31). Pengfei Tian was partially supported by the National Natural Science Foundation of China (41905017) and the Fundamental Research Funds for the Central Universities (lzujbky-2020-36). The authors acknowledge Jianjun Wang, Lijun Wang, and other staffs from the Ali Meteorological Administration for their help during the field campaign. The authors thank the NOAA for providing the HYSPLIT model (<https://ready.arl.noaa.gov/HYSPLIT.php>) and GDAS data (<https://www.ncep.noaa.gov/pmb/products/gfs/#GDAS>) and the NASA for providing the SRTM3 data (<http://www.jpl.nasa.gov/srtm/>).

### References

- Bian, J., Li, D., Bai, Z., Li, Q., Lyu, D., & Zhou, X. (2020). Transport of Asian surface pollutants to the global stratosphere from the Tibetan Plateau region during the Asian summer monsoon. *National Science Review*, 7(3), 516–533. <https://doi.org/10.1093/nsr/nwaa005>
- Cao, J., Tie, X., Xu, B., Zhao, Z., Zhu, C., Li, G., & Liu, S. (2011). Measuring and modeling black carbon (BC) contamination in the SE Tibetan Plateau. *Journal of Atmospheric Chemistry*, 67(1), 45. <https://doi.org/10.1007/s10874-011-9202-5>
- Cazorla, A., Bahadur, R., Suski, K. J., Cahill, J. F., Chand, D., Schmid, B., et al. (2013). Relating aerosol absorption due to soot, organic carbon, and dust to emission sources determined from in-situ chemical measurements. *Atmospheric Chemistry and Physics*, 13(18), 9337–9350. <https://doi.org/10.5194/acp-13-9337-2013>
- Che, H., Wang, Y., & Sun, J. (2011). Aerosol optical properties at Mt. Waliguan Observatory, China. *Atmospheric Environment*, 45(33), 6004–6009. <https://doi.org/10.1016/j.atmosenv.2011.07.050>
- Chen, P., Kang, S., Li, C., Zhang, Q., Guo, J., Tripathee, L., et al. (2019). Carbonaceous aerosol characteristics on the third pole: A primary study based on the atmospheric pollution and cryospheric change (APCC) network. *Environmental Pollution*, 253, 49–60. <https://doi.org/10.1016/j.envpol.2019.06.112>
- Chen, S., Huang, J., Zhao, C., Qian, Y., Leung, L. R., & Yang, B. (2013). Modeling the transport and radiative forcing of Taklimakan dust over the Tibetan Plateau: A case study in the summer of 2006. *Journal of Geophysical Research - D: Atmospheres*, 118, 797–812. <https://doi.org/10.1002/jgrd.50122>
- Cong, Z., Kang, S., Smirnov, A., & Holben, B. (2009). Aerosol optical properties at Nam Co, a remote site in central Tibetan Plateau. *Atmospheric Research*, 92(1), 42–48. <https://doi.org/10.1016/j.atmosres.2008.08.005>
- Cong, Z., Kawamura, K., Kang, S., & Fu, P. (2015). Penetration of biomass-burning emissions from South Asia through the Himalayas: New insights from atmospheric organic acids. *Scientific Reports*, 5(1), 9580. <https://doi.org/10.1038/srep09580>
- Deng, J., Zhang, Y., Hong, Y., Xu, L., Chen, Y., Du, W., & Chen, J. (2016). Optical properties of  $PM_{2.5}$  and the impacts of chemical compositions in the coastal city Xiamen in China. *Science of the Total Environment*, 557–558, 665–675. <https://doi.org/10.1016/j.scitotenv.2016.03.143>
- Du, W., Sun, Y. L., Xu, Y. S., Jiang, Q., Wang, Q. Q., Yang, W., et al. (2015). Chemical characterization of submicron aerosol and particle growth events at a national background site (3295 m a.s.l.) on the Tibetan Plateau. *Atmospheric Chemistry and Physics*, 15(18), 10811–10824. <https://doi.org/10.5194/acp-15-10811-2015>
- Dubovik, O., Holben, B., Eck, T. F., Smirnov, A., Kaufman, Y. J., King, M. D., et al. (2002). Variability of absorption and optical properties of key aerosol types observed in worldwide locations. *Journal of the Atmospheric Sciences*, 59(3), 590–608. [https://doi.org/10.1175/1520-0469\(2002\)059<0590:VOAAOP>2.0.CO;2](https://doi.org/10.1175/1520-0469(2002)059<0590:VOAAOP>2.0.CO;2)
- Garland, R. M., Yang, H., Schmid, O., Rose, D., Nowak, A., Aichtert, P., et al. (2008). Aerosol optical properties in a rural environment near the mega-city Guangzhou, China: Implications for regional air pollution, radiative forcing and remote sensing. *Atmospheric Chemistry and Physics*, 8(17), 5161–5186. <https://doi.org/10.5194/acp-8-5161-2008>

- Guinot, B., Cachier, H., & Oikonomou, K. (2007). Geochemical perspectives from a new aerosol chemical mass closure. *Atmospheric Chemistry and Physics*, 7(6), 1657–1670. <https://doi.org/10.5194/acp-7-1657-2007>
- Haywood, J., & Boucher, O. (2000). Estimates of the direct and indirect radiative forcing due to tropospheric aerosols: A review. *Reviews of Geophysics*, 38(4), 513–543. <https://doi.org/10.1029/1999RG000078>
- Hu, X., Zhang, Y., Ding, Z., Wang, T., Lian, H., Sun, Y., & Wu, J. (2012). Bioaccessibility and health risk of arsenic and heavy metals (Cd, Co, Cr, Cu, Ni, Pb, Zn and Mn) in TSP and PM<sub>2.5</sub> in Nanjing, China. *Atmospheric Environment*, 57, 146–152. <https://doi.org/10.1016/j.atmosenv.2012.04.056>
- Hu, Z., Huang, J., Zhao, C., Jin, Q., Ma, Y., & Yang, B. (2020). Modeling dust sources, transport, and radiative effects at different altitudes over the Tibetan Plateau. *Atmospheric Chemistry and Physics*, 20(3), 1507–1529. <https://doi.org/10.5194/acp-20-1507-2020>
- Huang, J., Minnis, P., Yi, Y., Tang, Q., Wang, X., Hu, Y., et al. (2007). Summer dust aerosols detected from CALIPSO over the Tibetan Plateau. *Geophysical Research Letters*, 34(18), L18805. <https://doi.org/10.1029/2007GL029938>
- Ji, Z., Kang, S., Cong, Z., Zhang, Q., & Yao, T. (2015). Simulation of carbonaceous aerosols over the Third Pole and adjacent regions: Distribution, transportation, deposition, and climatic effects. *Climate Dynamics*, 45(9), 2831–2846. <https://doi.org/10.1007/s00382-015-2509-1>
- Jia, A., Liang, S., Wang, D., Jiang, B., & Zhang, X. (2020). Air pollution slows down surface warming over the Tibetan Plateau. *Atmospheric Chemistry and Physics*, 20(2), 881–899. <https://doi.org/10.5194/acp-20-881-2020>
- Jin, M. (2006). MODIS observed seasonal and interannual variations of atmospheric conditions associated with hydrological cycle over Tibetan Plateau. *Geophysical Research Letters*, 33(19), L19707. <https://doi.org/10.1029/2006GL026713>
- Kandler, K., Schütz, L., Deutscher, C., Ebert, M., Hofmann, H., Jäckel, S., et al. (2009). Size distribution, mass concentration, chemical and mineralogical composition and derived optical parameters of the boundary layer aerosol at Tinfou, Morocco, during SAMUM 2006. *Tellus B: Chemical and Physical Meteorology*, 61(1), 32–50. <https://doi.org/10.1111/j.1600-0889.2008.00385.x>
- Kang, S., Chen, P., Li, C., Liu, B., & Cong, Z. (2016). Atmospheric aerosol elements over the inland Tibetan Plateau: Concentration, seasonality, and transport. *Aerosol and Air Quality Research*, 16(3), 789–800. <https://doi.org/10.4209/aaqr.2015.05.0307>
- Kang, S., Zhang, Q., Qian, Y., Ji, Z., Li, C., Cong, Z., et al. (2019). Linking atmospheric pollution to cryospheric change in the Third Pole region: Current progress and future prospects. *National Science Review*, 6(4), 796–809. <https://doi.org/10.1093/nsr/nwz031>
- Lau, K. M., Kim, M. K., & Kim, K. M. (2006). Asian summer monsoon anomalies induced by aerosol direct forcing: The role of the Tibetan Plateau. *Climate Dynamics*, 26(7), 855–864. <https://doi.org/10.1007/s00382-006-0114-z>
- Lau, W. K., Kim, M. K., Kim, K. M., & Lee, W. S. (2010). Enhanced surface warming and accelerated snow melt in the Himalayas and Tibetan Plateau induced by absorbing aerosols. *Environmental Research Letters*, 5(2), 025204. <https://doi.org/10.1088/1748-9326/5/2/025204>
- Li, C., Bosch, C., Kang, S., Andersson, A., Chen, P., Zhang, Q., et al. (2016). Sources of black carbon to the Himalayan-Tibetan Plateau glaciers. *Nature Communications*, 7, 12574. <https://doi.org/10.1038/ncomms12574>
- Liu, B., Cong, Z., Wang, Y., Xin, J., Wan, X., Pan, Y., et al. (2017). Background aerosol over the Himalayas and Tibetan Plateau: Observed characteristics of aerosol mass loading. *Atmospheric Chemistry and Physics*, 17(1), 449–463. <https://doi.org/10.5194/acp-17-449-2017>
- Liu, Y., Sato, Y., Jia, R., Xie, Y., Huang, J., & Nakajima, T. (2015). Modeling study on the transport of summer dust and anthropogenic aerosols over the Tibetan Plateau. *Atmospheric Chemistry and Physics*, 15(21), 12581–12594. <https://doi.org/10.5194/acp-15-12581-2015>
- Liu, Y., Zhu, Q., Huang, J., Hua, S., & Jia, R. (2019). Impact of dust-polluted convective clouds over the Tibetan Plateau on downstream precipitation. *Atmospheric Environment*, 209, 67–77. <https://doi.org/10.1016/j.atmosenv.2019.04.001>
- Lyamani, H., Olmo, F., & Aladosboledas, L. (2008). Light scattering and absorption properties of aerosol particles in the urban environment of Granada, Spain. *Atmospheric Environment*, 42(11), 2630–2642. <https://doi.org/10.1016/j.atmosenv.2007.10.070>
- Müller, D., Lee, K.-H., Gasteiger, J., Tesche, M., Weinzierl, B., Kandler, K., et al. (2012). Comparison of optical and microphysical properties of pure Saharan mineral dust observed with AERONET Sun photometer, Raman lidar, and in situ instruments during SAMUM 2006. *Journal of Geophysical Research*, 117(D7), D07211. <https://doi.org/10.1029/2011JD016825>
- Malm, W. C., Sisler, J. F., Huffman, D., Eldred, R. A., & Cahill, T. A. (1994). Spatial and seasonal trends in particle concentration and optical extinction in the United States. *Journal of Geophysical Research*, 99(D1), 1347–1370. <https://doi.org/10.1029/93JD02916>
- Marazzan, G. M., Vaccaro, S., Valli, G., & Vecchi, R. (2001). Characterisation of PM10 and PM<sub>2.5</sub> particulate matter in the ambient air of Milan (Italy). *Atmospheric Environment*, 35(27), 4639–4650. [https://doi.org/10.1016/S1352-2310\(01\)00124-8](https://doi.org/10.1016/S1352-2310(01)00124-8)
- Maussion, F., Scherer, D., Mölg, T., Collier, E., Curio, J., & Finkelnburg, R. (2014). Precipitation seasonality and variability over the Tibetan Plateau as resolved by the high Asia reanalysis. *Journal of Climate*, 27(5), 1910–1927. <https://doi.org/10.1175/jcli-d-13-00282.1>
- Mehta, M., Singh, N., & Solanki, R. (2019). Changing aerosol loadings over Central Himalayan region (2007–2016) - A satellite perspective. *Atmospheric Environment*, 207, 117–128. <https://doi.org/10.1016/j.atmosenv.2019.03.024>
- Parajuli, S. P., Stenichkov, G. L., Ukhov, A., & Kim, H. (2019). Dust emission modeling using a new high-resolution dust source function in WRF-Chem with implications for air quality. *Journal of Geophysical Research - D: Atmospheres*, 124(17–18), 10109–10133. <https://doi.org/10.1029/2019jd030248>
- Parajuli, S. P., Zobeck, T. M., Kocurek, G., Yang, Z.-L., & Stenichkov, G. L. (2016). New insights into the wind-dust relationship in sand-blasting and direct aerodynamic entrainment from wind tunnel experiments. *Journal of Geophysical Research - D: Atmospheres*, 121(4), 1776–1792. <https://doi.org/10.1002/2015jd024424>
- Pepin, N., Bradley, R. S., Diaz, H. F., Baraer, M., Caceres, N., Forsythe, H., et al. (2015). Elevation-dependent warming in mountain regions of the world. *Nature Climate Change*, 5(5), 424–430. <https://doi.org/10.1038/nclimate2563>
- Pokharel, M., Guang, J., Liu, B., Kang, S., Ma, Y., Holben, B. N., et al. (2019). Aerosol properties over Tibetan Plateau From a decade of AERONET measurements: Baseline, types, and influencing factors. *Journal of Geophysical Research - D: Atmospheres*, 124(23), 13357–13374. <https://doi.org/10.1029/2019JD031293>
- Reid, J. S., Jonsson, H. H., Maring, H. B., Smirnov, A., Savoie, D. L., Cliff, S. S., et al. (2003). Comparison of size and morphological measurements of coarse mode dust particles from Africa. *Journal of Geophysical Research*, 108(D19), 8593. <https://doi.org/10.1029/2002JD002485>
- Retama, A., Baumgardner, D., Raga, G. B., McMeeking, G. R., & Walker, J. W. (2015). Seasonal and diurnal trends in black carbon properties and co-pollutants in Mexico City. *Atmospheric Chemistry and Physics*, 15(16), 9693–9709. <https://doi.org/10.5194/acp-15-9693-2015>
- Sciare, J., Oikonomou, K., Cachier, H., Mihalopoulos, N., Andreae, M. O., Maenhaut, W., & Sarda-Estève, R. (2005). Aerosol mass closure and reconstruction of the light scattering coefficient over the Eastern Mediterranean Sea during the MINOS campaign. *Atmospheric Chemistry and Physics*, 5(8), 2253–2265. <https://doi.org/10.5194/acp-5-2253-2005>
- Selimovic, V., Yokelson, R. J., Warneke, C., Roberts, J. M., de Gouw, J., Reardon, J., & Griffith, D. W. T. (2018). Aerosol optical properties and trace gas emissions by PAX and OP-FTIR for laboratory-simulated western US wildfires during FIREX. *Atmospheric Chemistry and Physics*, 18(4), 2929–2948. <https://doi.org/10.5194/acp-18-2929-2018>

- Shang, D., Hu, M., Zheng, J., Qin, Y., Du, Z., Li, M., et al. (2018). Particle number size distribution and new particle formation under the influence of biomass burning at a high altitude background site at Mt. Yulong (3410 m), China. *Atmospheric Chemistry and Physics*, 18(21), 15687–15703. <https://doi.org/10.5194/acp-18-15687-2018>
- Shao, Y. (2008). *Physics and modelling of wind erosion*. Dordrecht: Springer.
- Sow, M., Alfaro, S. C., Rajot, J. L., & Marticorena, B. (2009). Size resolved dust emission fluxes measured in Niger during 3 dust storms of the AMMA experiment. *Atmospheric Chemistry and Physics*, 9(12), 3881–3891. <https://doi.org/10.5194/acp-9-3881-20>
- Tian, P., Cao, X., Zhang, L., Sun, N., Sun, L., Logan, T., et al. (2017). Aerosol vertical distribution and optical properties over China from long-term satellite and ground-based remote sensing. *Atmospheric Chemistry and Physics*, 17(4), 2509–2523. <https://doi.org/10.5194/acp-17-2509-2017>
- Tian, P., Zhang, L., Ma, J., Tang, K., Xu, L., Wang, Y., et al. (2018). Radiative absorption enhancement of dust mixed with anthropogenic pollution over East Asia. *Atmospheric Chemistry and Physics*, 18(11), 7815–7825. <https://doi.org/10.5194/acp-18-7815-2018>
- Turpin, B. J., & Lim, H.-J. (2001). Species Contributions to PM<sub>2.5</sub> mass concentrations: Revisiting common assumptions for estimating organic mass. *Aerosol Science and Technology*, 35(1), 602–610. <https://doi.org/10.1080/02786820119445>
- Wan, X., Kang, S., Xin, J., Liu, B., Wen, T., Wang, P., et al. (2016). Chemical composition of size-segregated aerosols in Lhasa city, Tibetan Plateau. *Atmospheric Research*, 174–175, 142–150. <https://doi.org/10.1016/j.atmosres.2016.02.005>
- Wang, T., Chen, Y., Gan, Z., Han, Y., Li, J., & Huang, J. (2020). Assessment of dominating aerosol properties and their long-term trend in the Pan-Third Pole region: A study with 10-year multi-sensor measurements. *Atmospheric Environment*, 239, 117738. <https://doi.org/10.1016/j.atmosenv.2020.117738>
- Wang, X., Wen, H., Shi, J., Bi, J., Huang, Z., Zhang, B., et al. (2018). Optical and microphysical properties of natural mineral dust and anthropogenic soil dust near dust source regions over northwestern China. *Atmospheric Chemistry and Physics*, 18(3), 2119–2138. <https://doi.org/10.5194/acp-18-2119-2018>
- Wang, Y., Hu, M., Lin, P., Tan, T., Li, M., Xu, N., et al. (2019). Enhancement in particulate organic nitrogen and light absorption of humic-like substances over Tibetan Plateau due to long-range transported biomass burning emissions. *Environmental Science & Technology*, 53(24), 14222–14232. <https://doi.org/10.1021/acs.est.9b06152>
- Wang, Y., Jia, C., Tao, J., Zhang, L., Liang, X., Ma, J., et al. (2016). Chemical characterization and source apportionment of PM<sub>2.5</sub> in a semi-arid and petrochemical-industrialized city, Northwest China. *Science of the Total Environment*, 573, 1031–1040. <https://doi.org/10.1016/j.scitotenv.2016.08.179>
- Watson, J. G., Chow, J. C., & Houck, J. E. (2001). PM<sub>2.5</sub> chemical source profiles for vehicle exhaust, vegetative burning, geological material, and coal burning in Northwestern Colorado during 1995. *Chemosphere*, 43(8), 1141–1151. [https://doi.org/10.1016/S0045-6535\(00\)00171-5](https://doi.org/10.1016/S0045-6535(00)00171-5)
- Xia, X., Wang, P., Wang, Y., Li, Z., Xin, J., Liu, J., & Chen, H. (2008). Aerosol optical depth over the Tibetan Plateau and its relation to aerosols over the Taklimakan Desert. *Geophysical Research Letters*, 35(16), L16804. <https://doi.org/10.1029/2008GL034981>
- Xing, L., Fu, T. M., Cao, J., Lee, S. C., Wang, G., Ho, K., et al. (2013). Seasonal and spatial variability of the OM/OC mass ratios and high regional correlation between oxalic acid and zinc in Chinese urban organic aerosols. *Atmospheric Chemistry and Physics*, 13(8), 4307–4318. <https://doi.org/10.5194/acp-13-4307-2013>
- Xiong, J., Zhao, T., Liu, Y., Han, Y., Liu, F., & Li, J. (2016). Sensitivity simulation of contribution of desertification over Qinghai-Xizang Plateau to East Asian dust aerosols. *Plateau Meteorology*, 35(3), 590–596. <https://doi.org/10.7522/j.issn.1000-0534.2015.00024>
- Xu, C., Ma, Y., Yang, K., & You, C. (2018). Tibetan Plateau impacts on global dust transport in the upper troposphere. *Journal of Climate*, 31(12), 4745–4756. <https://doi.org/10.1175/JCLI-D-17-0313.1>
- Xu, J., Hettiyadura, A. P. S., Liu, Y., Zhang, X., Kang, S., & Laskin, A. (2020). Regional differences of chemical composition and optical properties of aerosols in the Tibetan Plateau. *Journal of Geophysical Research: Atmospheres*, 125(1), e2019JD031226. <https://doi.org/10.1029/2019JD031226>
- Xu, J., Zhang, Q., Shi, J., Ge, X., Xie, C., Wang, J., et al. (2018). Chemical characteristics of submicron particles at the central Tibetan Plateau: Insights from aerosol mass spectrometry. *Atmospheric Chemistry and Physics*, 18(1), 427–443. <https://doi.org/10.5194/acp-18-427-2018>
- Xu, J., Zhang, Q., Wang, Z., Yu, G., Ge, X., & Qin, X. (2015). Chemical composition and size distribution of summertime PM<sub>2.5</sub> at a high altitude remote location in the northeast of the Qinghai-Xizang (Tibet) Plateau: Insights into aerosol sources and processing in free troposphere. *Atmospheric Chemistry and Physics*, 15(9), 5069–5081. <https://doi.org/10.5194/acp-15-5069-2015>
- Yan, N., Wu, G., Zhang, X., Zhang, C., Xu, T., & Lazhu, (2015). Variation of aerosol optical properties from AERONET observation at Mt. Muztagh Ata, Eastern Pamirs. *Atmospheric Research*, 153, 480–488. <https://doi.org/10.1016/j.atmosres.2014.10.013>
- Yang, J., Kang, S., Ji, Z., & Chen, D. (2018). Modeling the origin of anthropogenic black carbon and its climatic effect over the Tibetan plateau and surrounding regions. *Journal of Geophysical Research - D: Atmospheres*, 123(2), 671–692. <https://doi.org/10.1002/2017jd027282>
- Yao, T., Xue, Y., Chen, D., Chen, F., Thompson, L., Cui, P., et al. (2019). Recent Third Pole's rapid warming accompanies cryospheric melt and water cycle intensification and interactions between monsoon and environment: Multidisciplinary approach with observations, modeling, and analysis. *Bulletin of the American Meteorological Society*, 100(3), 423–444. <https://doi.org/10.1175/BAMS-D-17-0057.1>
- Yu, Y., Zhao, S., Wang, B., Fu, P., & He, J. (2017). Pollution characteristics revealed by size distribution properties of aerosol particles at urban and suburban sites, northwest China. *Aerosol Air Quality Research*, 17(7), 1784–1797. <https://doi.org/10.4209/aaqr.2016.07.0330>
- Zhang, N., Cao, J., Ho, K., & He, Y. (2012). Chemical characterization of aerosol collected at Mt. Yulong in wintertime on the southeastern Tibetan Plateau. *Atmospheric Research*, 107, 76–85. <https://doi.org/10.1016/j.atmosres.2011.12.012>
- Zhang, N., Cao, J., Liu, S., Zhao, Z., Xu, H., & Xiao, S. (2014). Chemical composition and sources of PM<sub>2.5</sub> and TSP collected at Qinghai Lake during summertime. *Atmospheric Research*, 138, 213–222. <https://doi.org/10.1016/j.atmosres.2013.11.016>
- Zhang, N., Cao, J., Wang, Q., Huang, R., Zhu, C., Xiao, S., & Wang, L. (2018). Biomass burning influences determination based on PM 2.5 chemical composition combined with fire counts at southeastern Tibetan Plateau during pre-monsoon period. *Atmospheric Research*, 206, 108–116. <https://doi.org/10.1016/j.atmosres.2018.02.018>
- Zhang, X., Mao, M., Chen, H., & Tang, S. (2020). Theoretical study of scattering Angstrom exponent of coated black carbon aerosols: The effect of microphysical configurations. *Journal of Quantitative Spectroscopy and Radiative Transfer*, 256, 107302. <https://doi.org/10.1016/j.jqsrt.2020.107302>
- Zhang, X., Ming, J., Li, Z., Wang, F., & Zhang, G. (2017). The online measured black carbon aerosol and source orientations in the Nam Co region, Tibet. *Environmental Science & Pollution Research*, 24(32), 25021–25033. <https://doi.org/10.1007/s11356-017-0165-1>
- Zhang, X., Xu, J., Kang, S., Liu, Y., & Zhang, Q. (2018). Chemical characterization of long-range transport biomass burning emissions to the Himalayas: Insights from high-resolution aerosol mass spectrometry. *Atmospheric Chemistry and Physics*, 18(7), 4617–4638. <https://doi.org/10.5194/acp-18-4617-2018>

- Zhang, X., Xu, J., Kang, S., Zhang, Q., & Sun, J. (2019). Chemical characterization and sources of submicron aerosols in the northeastern Qinghai-Tibet Plateau: Insights from high-resolution mass spectrometry. *Atmospheric Chemistry and Physics*, *19*(11), 7897–7911. <https://doi.org/10.5194/acp-19-7897-2019>
- Zhang, X. Y., Arimoto, R., Cao, J. J., An, Z. S., & Wang, D. (2001). Atmospheric dust aerosol over the Tibetan Plateau. *Journal of Geophysical Research*, *106*(D16), 18471–18476. <https://doi.org/10.1029/2000jd900672>
- Zhang, X. Y., Gong, S. L., Arimoto, R., Shen, Z. X., Mei, F. M., Wang, D., & Cheng, Y. (2003). Characterization and temporal variation of Asian dust aerosol from a site in the Northern Chinese deserts. *Journal of Atmospheric Chemistry*, *44*(3), 241–257. <https://doi.org/10.1023/A:1022900220357>
- Zhang, Y., Xu, J., Shi, J., Xie, C., Ge, X., Wang, J., et al. (2017). Light absorption by water-soluble organic carbon in atmospheric fine particles in the central Tibetan Plateau. *Environmental Science & Pollution Research*, *24*(26), 21386–21397. <https://doi.org/10.1007/s11356-017-9688-8>
- Zhao, C., Yang, Y., Fan, H., Huang, J., Fu, Y., Zhang, X., et al. (2019). Aerosol characteristics and impacts on weather and climate over the Tibetan Plateau. *National Science Review*, *7*(3), 492–495. <https://doi.org/10.1093/nsr/nwz184>
- Zhao, P., Xu, X., Chen, F., Guo, X., Zheng, X., Liu, L., et al. (2018). The third atmospheric scientific experiment for understanding the Earth-atmosphere coupled system over the Tibetan Plateau and its effects. *Bulletin of the American Meteorological Society*, *99*(4), 757–776. <https://doi.org/10.1175/bams-d-16-0050.1>
- Zhao, Z., Cao, J., Shen, Z., Xu, B., Zhu, C., Chen, L.-W. A., et al. (2013). Aerosol particles at a high-altitude site on the Southeast Tibetan Plateau, China: Implications for pollution transport from South Asia. *Journal of Geophysical Research - D: Atmospheres*, *118*, 360. <https://doi.org/10.1002/jgrd.50599>
- Zheng, J., Hu, M., Du, Z., Shang, D., Gong, Z., Qin, Y., et al. (2017). Influence of biomass burning from South Asia at a high-altitude mountain receptor site in China. *Atmospheric Chemistry and Physics*, *17*(11), 6853–6864. <https://doi.org/10.5194/acp-17-6853-2017>
- Zhu, C., Cao, J., Ho, K., Antony Chen, L. W., Huang, R., Wang, Y., et al. (2015). The optical properties of urban aerosol in northern China: A case study at Xi'an. *Atmospheric Research*, *160*, 59–67. <https://doi.org/10.1016/j.atmosres.2015.03.008>
- Zhu, J., Xia, X., Che, H., Wang, J., Cong, Z., Zhao, T., et al. (2019). Spatiotemporal variation of aerosol and potential long-range transport impact over the Tibetan Plateau, China. *Atmospheric Chemistry and Physics*, *19*(23), 14637–14656. <https://doi.org/10.5194/acp-19-14637-2019>